

# Environmental structuring of marine plankton phenology

Daniel G. Boyce<sup>1,2\*</sup>, Brian Petrie<sup>2</sup>, Kenneth T. Frank<sup>2</sup>, Boris Worm<sup>3</sup> and William C. Leggett<sup>1</sup>

**Seasonal cycles of primary production (phenology) critically influence biogeochemical cycles, ecosystem structure and climate. In the oceans, primary production is dominated by microbial phytoplankton that drift with currents, and show rapid turnover and chaotic dynamics, factors that have hindered understanding of their phenology. We used all available observations of upper-ocean phytoplankton concentration (1995–2015) to describe global patterns of phytoplankton phenology, the environmental factors that structure them, and their relationships to terrestrial patterns. Phytoplankton phenologies varied strongly by latitude and productivity regime: those in high-production regimes were governed by insolation, whereas those in low-production regimes were constrained by vertical mixing. In eight of ten ocean regions, our findings contradict the hypothesis that phytoplankton phenologies are coherent at basin scales. Lastly, the spatial organization of phenological patterns in the oceans was broadly similar to those on land, suggesting an overarching effect of insolation on the phenology of primary producers globally.**

The phenology of primary producers drives seasonal fluctuations in atmospheric<sup>1</sup> and oceanic<sup>2</sup> carbon dioxide concentration, affects the biogeochemical cycling of carbon and nutrients<sup>3</sup>, and can have profound effects on the movement<sup>4</sup>, reproduction<sup>5</sup> and survivorship<sup>6</sup> of consumers. Variation in phenology among species also helps to maintain species coexistence<sup>7</sup> and local biodiversity, with consequences for the structure and functioning of ecosystems<sup>8</sup>. Phenology accounts for a dominant fraction of the temporal variability of primary producer biomass<sup>9</sup>, and its accurate representation is necessary to reliably estimate time trends in biomass<sup>10–13</sup>. Consequently, the phenology of primary producers is an informative indicator of ecosystem status.

Several studies of terrestrial vegetation have reported that phenology is shifting regionally and globally in response to climate change<sup>14–16</sup>. Oceanic primary production is of similar magnitude to that on land<sup>17</sup>, yet surprisingly little is understood of how marine phenologies are arranged and structured. In sharp contrast to terrestrial primary producers which are large, sessile, slow-growing and patchily distributed, marine production is dominated by single-celled phytoplankton (0.2–200 µm), which are of diverse taxonomic origin, drift over large distances, have a rapid turnover time (2–6 days)<sup>18</sup> and can exhibit chaotic dynamics<sup>19</sup>. These striking differences may explain the paucity of studies of marine phytoplankton phenology at global scales<sup>20–23</sup>, and why we lack a fundamental understanding of how their phenologies are arranged and structured across the seascape. Given the mounting evidence that biogeographical patterns in the biomass<sup>10,11</sup>, size structure<sup>24</sup> and community composition<sup>13</sup> of marine phytoplankton are changing globally, an improved understanding of phytoplankton phenology, which strongly influences these factors, is required.

We used all available observations of marine phytoplankton concentration between 1995 and 2015 to explore the global biogeography of their phenology and the environmental factors that structure them. The database includes observations of upper-ocean chlorophyll, ocean colour and transparency, collected by satellite and ship-board sampling platforms (Supplementary Table 1). We used a new analytical approach that independently estimated seasonal cycles

from up to five different observation types using statistical models and then standardized and integrated these phenologies using multi-model inference<sup>25</sup>.

Variation in phytoplankton phenology has been linked to factors influencing biomass production, notably the availability of critical resources such as nutrients<sup>11,26</sup> and insolation<sup>18</sup>, and to factors affecting mortality such as grazing. We used variables that act as proxies for these: sea surface temperature (SST), surface wind speed ( $\text{m s}^{-1}$ ), vertical stratification ( $\text{kg m}^{-3}$ ), nitrate concentration ( $\mu\text{mol l}^{-1}$ ), fractional cloud cover (%), daylight duration (h) and zooplankton abundance (Supplementary Table 1). The influence of these biotic and abiotic drivers on marine phenology was explored using techniques and statistical modelling<sup>27</sup>.

The production of marine and terrestrial vegetative biomass is well known to be driven by common requirements for light and nutrients. However, whereas insolation, nitrate and iron are predominant drivers in the oceans, water availability and temperature impose additional constraints on land<sup>28</sup>. Irrespective of the large differences in the space and timescales at which marine and terrestrial primary producers operate, their overlapping resource requirements create the potential for global synchrony in their phenologies. We evaluated this hypothesis by estimating phenologies in terrestrial systems using the Normalized Difference Vegetation Index (NDVI) and comparing them to phenologies in the oceans.

## Results

**Data and approach.** Individual observations in the phytoplankton database were projected onto a global equal-area grid of 48 by 88 cells, and grouped into five distinct data types, which were identified by the measurement units and observational platforms used (see Methods and Supplementary Table 1). For each unique equal-area grid cell (G) and data type (D), a single seasonal cycle in phytoplankton concentration was estimated, hereafter referred to as a phenocycle<sub>G,D</sub>, by using generalized additive models<sup>29</sup> (GAMs). This methodology extends recently developed generalized linear model approaches that have a limited capacity to approximate the cyclic nonlinear variability of phenological cycles<sup>23,30</sup>. The predicted values

<sup>1</sup>Department of Biology, Queen's University, Kingston, ON K7L 3N6, Canada. <sup>2</sup>Ocean Sciences Division, Bedford Institute of Oceanography, PO Box 1006, Dartmouth, NS B2Y 4A2, Canada. <sup>3</sup>Department of Biology, Dalhousie University, Halifax, NS B3H 4R2, Canada. \*e-mail: [Dgb1@queensu.ca](mailto:Dgb1@queensu.ca)

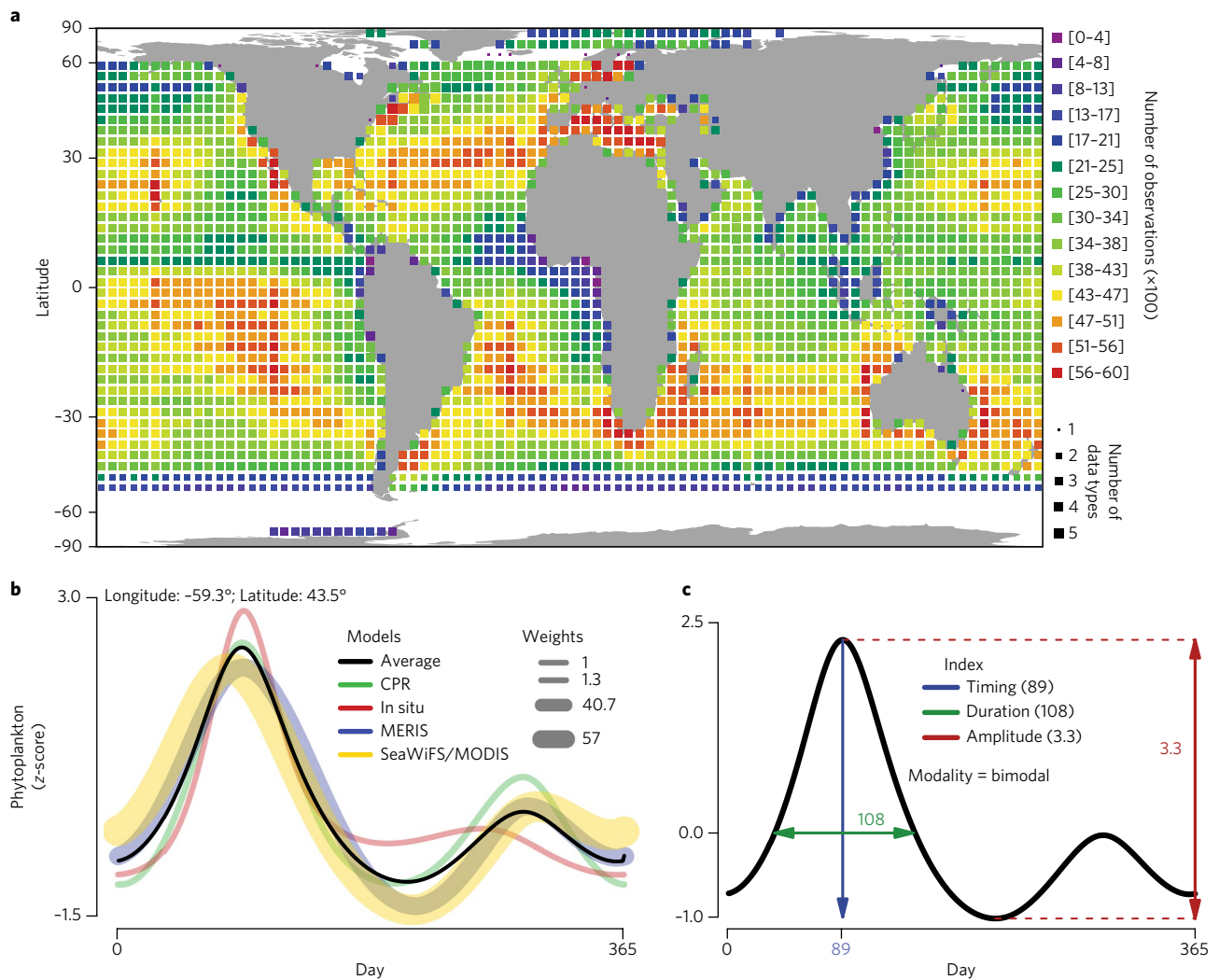


**Fig. 1 | Data availability and modelling approach. a**, Spatial distribution of observations used in the phenology estimation. Colours and symbol sizes depict the total number of observations and number of data types available in each equal-area grid cell, respectively. **b**, An example of the multi-model inference procedure. Coloured trend lines are the phenocycles<sub>G,D</sub> estimated from each different data type within an example grid cell, and the black trend line is the multi-model ensemble average. The colour depicts the data type, and the line thickness depicts the standardized model weight, where large values denote models with a greater information-theoretic weight. MERIS, Medium Resolution Imaging Spectrometer. **c**, An example of the derivation of phenology indices for the multi-model averaged phenocycle from panel **b**. The main indices of phenology are the timing of the maximum (blue), its duration (green) and amplitude (red). The estimation of modality is also reported.

of each phenocycle<sub>G,D</sub> were transformed into standardized units of variance (see equation (2) in the Methods section).

We removed all phenocycles<sub>G,D</sub> that failed to meet the minimum data-sufficiency criteria as objectively determined through simulation analyses (see Methods section and Supplementary Information). This procedure yielded 5,574 individual phenocycles<sub>G,D</sub> (Fig. 1a). Observation density was greatest at mid-latitudes (20°–50° N and S), particularly in nearshore waters around North America and Europe. Fewer observations were available at higher latitudes, particularly in the Southern and North Indian Oceans (Fig. 1a). Most phenocycles<sub>G,D</sub> were derived using data from remote-sensing platforms, but shipboard sampling provided coverage at high latitudes where satellite coverage is poor<sup>31</sup>. Phenocycles<sub>G,D</sub> were predominantly estimated from time-series containing at least 11 months of observations, and for which the longest stretch of missing observations was <10 days.

For each grid cell, the standardized phenocycles<sub>G,D</sub> were integrated across the different data types using multi-model averaging<sup>25</sup>. Phenocycles<sub>G,D</sub> derived from the highest information-theoretic

ranked models were given greater influence in the multi-model average<sup>25</sup> (Fig. 1b and Supplementary Fig. 1). This procedure yielded a standardized, multi-model averaged phenocycle (hereafter phenocycle<sub>A</sub>) for each of 2,822 grid cells that collectively accounted for 94% of the surface area of the global ocean. Each phenocycle<sub>A</sub> was standardized to account for latitudinal variability in seasonal insolation to enable comparisons between Northern and Southern Hemisphere cycles. This objective was achieved by adjusting the temporal axis of each phenocycle<sub>A</sub> so that it was centred on the day on which the peak duration of daylight hours occurred (day 0), yielding a standard annual scale from day –182.5 to 182.5 (hereafter day<sub>DL</sub>). We then described global spatial patterns of phenology by estimating the timing, amplitude, duration and modality of each phenocycle<sub>A</sub> (see Methods section and Fig. 1c). The complete analysis workflow is depicted in Supplementary Fig. 1.

**Phenology patterns.** We adopted the approach of ref. <sup>22</sup>, which was based on fuzzy clustering<sup>32</sup>, to characterize the similarity between the phenocycles<sub>A</sub>. Five clusters produced an optimal separation

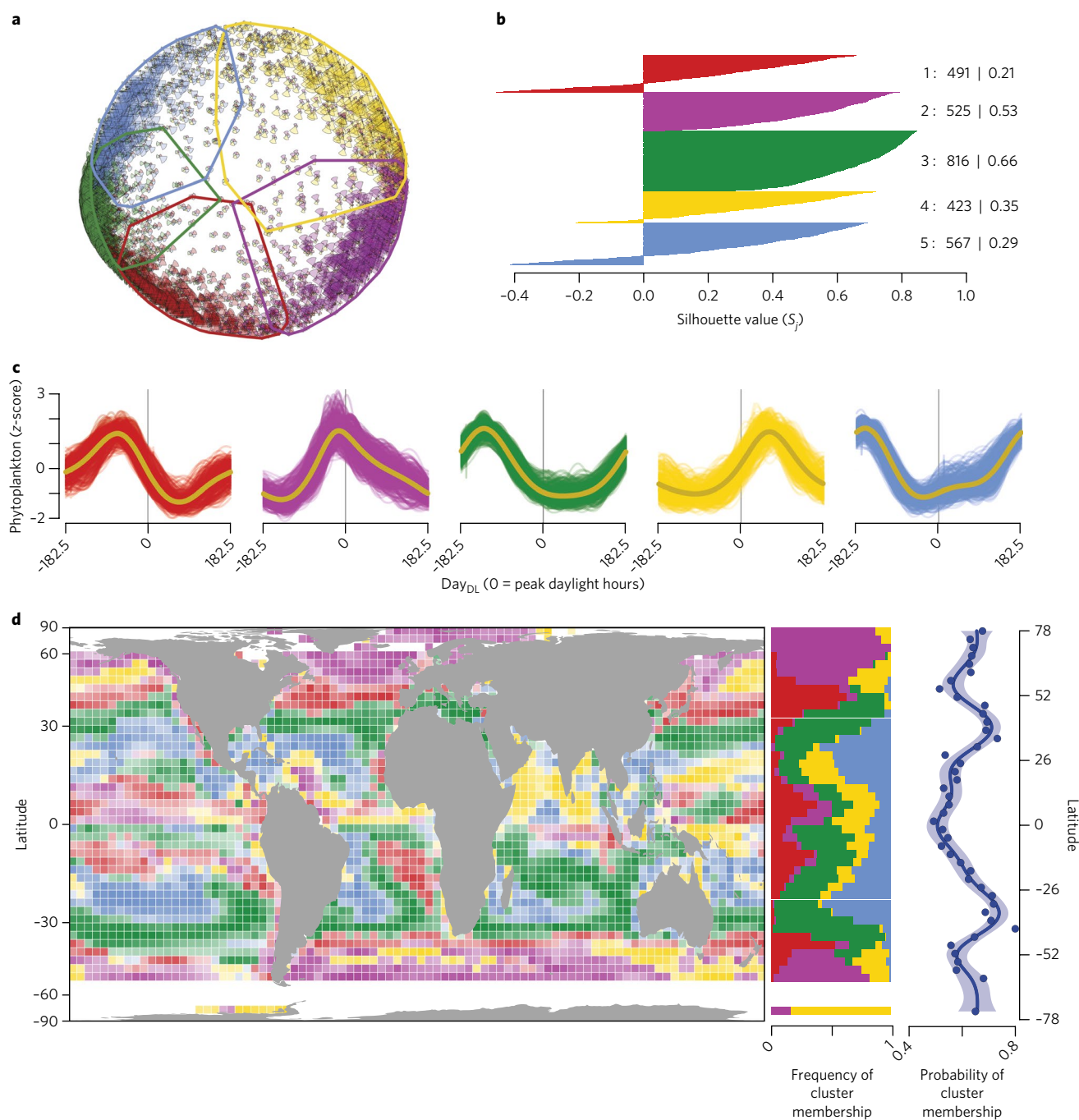


**Fig. 2 | Global patterns of phytoplankton phenology.** **a**, Fuzzy clustering of phytoplankton phenocycles. Each point depicts a phenocycle<sub>A</sub> from a single grid cell. Colours depict the five different phenological patterns (clusters) identified; the location depicts the relative similarity of the phenocycles<sub>A</sub>. The size and shading of the points represent the probability of cluster membership, where large opaque points have a higher probability of cluster membership. **b**, Estimated silhouette values for each cluster. Larger values indicate a high degree of similarity within clusters. The number of phenocycles and average silhouette value for each cluster are displayed in the right margin. **c**, Annual variability in standardized phytoplankton anomalies for each cluster. Semi-transparent coloured lines are the estimated phenocycles<sub>A</sub> from each grid cell. Colours identify the clusters described in **a** and **b**; thick dark yellow lines depict the average of all phenocycles<sub>A</sub> within each cluster. The vertical line depicts the timing of the peak daylight duration. **d**, Spatial distribution of the clusters. Colours depict the cluster membership, and transparency depicts the probability of cluster membership; opaque represents high probability. Bars in the right margin depict the frequency of occurrence of each cluster by latitude. Points and trend line in the right margin depict the average probability of cluster membership by latitude.

in multivariate space and captured distinctive phenology patterns (Fig. 2a). Silhouette values ( $S_j$ ) were estimated for each phenocycle<sub>A</sub> (equation (8)) to quantify the degree of within-cluster similarity. Values of  $S_j$  ranged between  $-1$  and  $1$ , with high values denoting greater within-cluster similarity. Average silhouette

values for each of the five clusters ranged between  $0.21$  and  $0.66$  (Fig. 2b). Phenocycles<sub>A</sub> within each of the five clusters exhibited a single dominant peak, but different amplitude, duration and timing (Fig. 2c). Smaller secondary peaks (bimodality) were present in  $50.3\%$  of all phenocycles<sub>A</sub>. The green cluster (Fig. 2) contained most

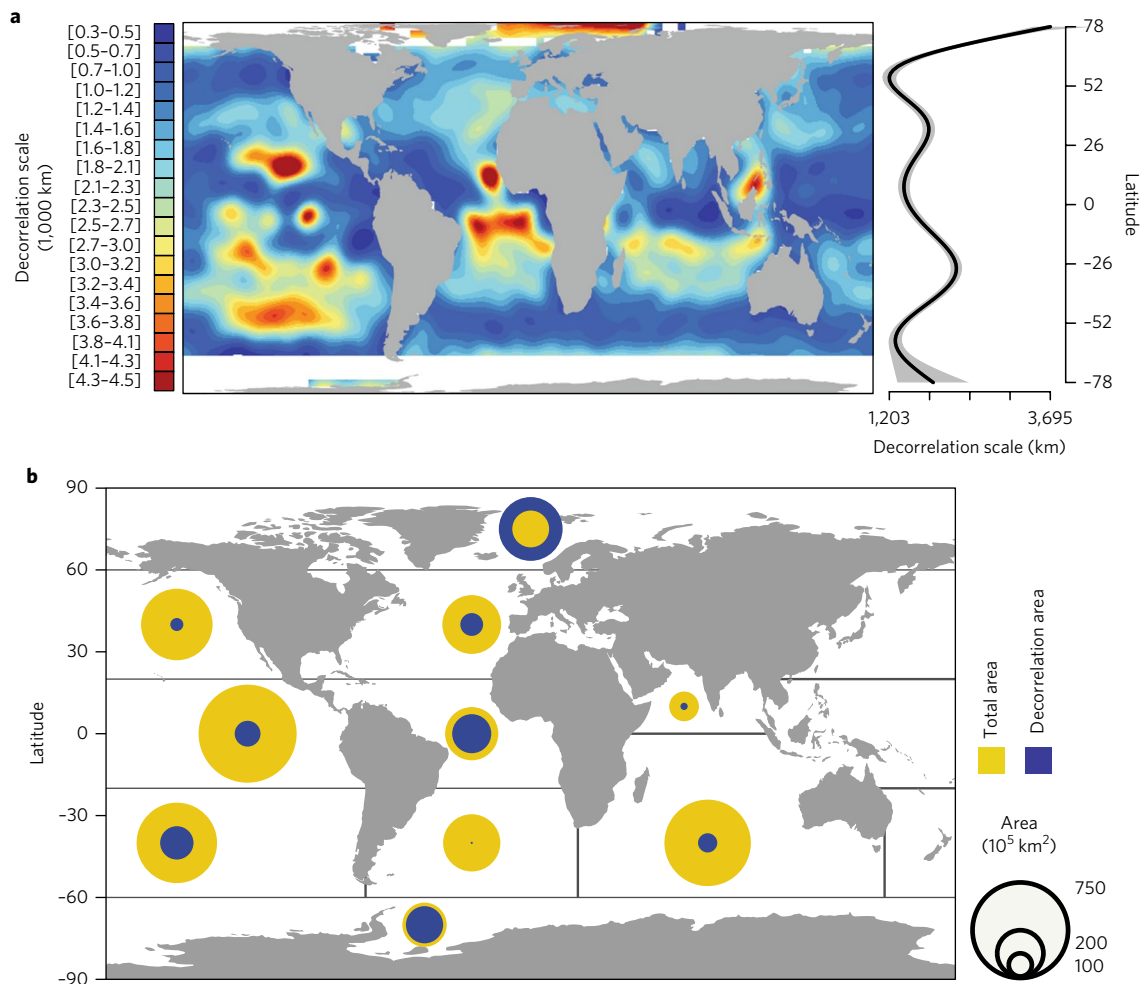


**Fig. 3 | Spatial synchrony of phytoplankton phenology.** **a**, Estimated decorrelation scale of all phenocycles<sub>A</sub> calculated for each grid cell. Colours depict the distance at which the correlation between phenocycles<sub>A</sub> decays to  $e^{-1}$ . Dark blue depicts short decorrelation distances, and dark red depicts long distances that signify more homogeneous spatial patterns. The values were spatially interpolated using a GAM (see Supplementary Information for mapped discrete values). The inset depicts the predicted mean decorrelation distance along latitude. The black line is the mean decorrelation distance predicted from an inverse-variance-weighted GAM; shading depicts the 95% confidence interval around the mean. **b**, Average omnidirectional phenocycle<sub>A</sub> decorrelation area, relative to the total area, within ten large ocean regions. Black lines denote the boundaries of the ten ocean areas as defined in ref. <sup>11</sup>. Blue depicts the phenocycle<sub>A</sub> decorrelation area and yellow depicts the total area within each of the ten regions.

of the phenocycles<sub>A</sub> ( $N=816$ ; 29%), was well defined by the clustering ( $S_j=0.66$ ) and had the greatest proportion of unimodal phenocycles<sub>A</sub> (76%). The red ( $N=491$ ; 17%) and light blue ( $N=567$ ; 20%) clusters were closely related to the green, and their cluster assignments were weaker (red  $S_j=0.21$ ; blue  $S_j=0.29$ ). The purple cluster ( $N=525$ ; 19%) was well defined ( $S_j=0.53$ ), and the timing of its maximum was most closely aligned with peak daylight duration. The yellow cluster was weakly defined ( $S_j=0.35$ ) and was least commonly observed globally ( $N=423$ ; 15%), except in the northern Indian Ocean, where it predominated. Cluster-averaged phenocycles (Fig. 2c; dark yellow lines) were unimodal and largely distinguished according to their timing.

Over the extratropical oceans ( $>10^\circ$  N and S), phenology cluster assignments showed clear latitudinal patterns (Fig. 2d). High-latitude clusters ( $>50^\circ$  N and S) were synchronous with the timing of peak insolation (purple), whereas lower latitude ( $10^\circ$ – $30^\circ$  N and S) clusters were weakly synchronous (blue). The probability of membership was greatest at mid-latitudes, indicative of well-defined clustering of the phenocycles<sub>A</sub> there (Fig. 2d). Low-latitude ( $<10^\circ$  N and S) phenocycles<sub>A</sub> were weakly defined, with all five clusters being approximately equally distributed there (Fig. 2d). Variable low-latitude

phenologies have been observed previously<sup>33</sup> and are hypothesized to be driven by the latitudinally dependent effects of wind stress on vertical mixing<sup>34</sup>. At low latitudes, relatively small changes in wind stress can induce complex, spatially differential responses in vertical mixing and nutrient delivery, manifesting as spatially and temporally variable phytoplankton bloom dynamics<sup>34</sup>.

Our identification of five phenology patterns differs from previous reports of six<sup>20,22</sup> or eight<sup>23</sup>. These differences may stem from limitations in the spatial extent of previous analyses, or from differences in approach. Our incorporation of multiple data types made a more global analysis possible, encompassing high-latitude locations ( $>60^\circ$  N and S), where satellite observations are often lacking<sup>20,22,31</sup>. Our analysis also aided interpretation of phenological cycles independently of the average phytoplankton biomass level, and of the timing of seasonal insolation, both of which can bias estimates of the amplitude and timing of phenology<sup>21,23</sup>.

**Spatial scales of phenology.** We quantified the spatial scales over which phenocycles<sub>A</sub> were coherent by estimating the decorrelation scale for each grid cell (see Methods section). The greatest omnidirectional distances over which phenocycles<sub>A</sub> were coherent

(>4,000 km) occurred in the Arctic Ocean and at localized areas within the temperate (20°–40° N and S) eastern Pacific, Atlantic and Southern Indian Oceans (Fig. 3a). The shortest decorrelation scales (<1,000 km) were observed at low latitudes (<10° N and S) of the Pacific, Indian and western Atlantic Oceans, and within temperate high latitudes (50°–60° N and S) of the North Pacific, South Atlantic and Indian Oceans. The decorrelation scales of phenocycles<sub>A</sub> were negatively related to the average phytoplankton concentration within each grid cell ( $r = -0.22$ ;  $P < 0.0001$ ; Supplementary Fig. 8b). This global relationship suggests that phenocycles<sub>A</sub> are uniform over large geographical areas in low-productivity regimes such as in the oligotrophic gyres, and more spatially variable in highly productive regimes such as nearshore waters.

The decorrelation scales were longer and less variable when calculated along strictly longitudinal directions (median = 4,256 km; s.d. = 2,789 km), relative to those calculated along strictly latitudinal directions (median = 952 km; s.d. = 919 km; Supplementary Fig. 9). Estimating the decorrelation distances in the four cardinal directions (north, east, south and west) revealed clear spatial dependence in the directionality of phenology decorrelation, which may be related to the major surface currents of the oceans<sup>35</sup> (Supplementary Fig. 10). The maximum decorrelation scales were frequently perpendicular to major surface currents, most notably the Antarctic circumpolar current (at about 45°–55° S) and equatorial countercurrent (at about 0°). The scaled symmetry of the decorrelation scales was greatest within oceanic gyres where currents are relatively weak, with the grid cells surrounding the gyres exhibiting asymmetric decorrelation scales oriented towards the gyre centre.

We tested the common assumption<sup>11,12,36,37</sup> that phenocycles<sub>A</sub> are uniform at the scale of ocean basins. To do so, we calculated the omnidirectional areal decorrelation scale of the phenocycles<sub>A</sub> relative to the total area within ten ocean regions for which phenology has been assumed to be uniform. Excepting the Arctic and Southern Ocean regions, the decorrelation area of the phenocycles<sub>A</sub> was much less than the total area of the region (median: 24%; range: 14–64%; Fig. 3b). Based on these findings, we reject the assumption of a uniform phenology pattern at the scale of ocean basins.

**Environmental structuring.** We performed an unconstrained principal component analysis (PCA) to explore the associations between the environmental factors (SST, N, Chl, bathymetry, latitude, stratification, wind speed) and the simultaneous linear relationships between all phenology indices (timing, duration, amplitude and modality). The first two principal components accounted for 67% of the variance and suggested that the phenology indices were best-associated with global productivity regimes, defined by their average chlorophyll levels (Chl). In low-productivity regimes, as in the oligotrophic gyres (Chl < 0.07 mg m<sup>-3</sup>; Fig. 4a, blue ellipse and points), the timing of the phenocycle<sub>A</sub> maximum was synchronous with the timing of the minimum stratification. In highly productive regimes, such as high latitudes and nearshore waters (Chl > 0.25 mg m<sup>-3</sup>; Fig. 4a, green ellipse and points), the phenocycles<sub>A</sub> exhibited greater amplitude, and their maximum was synchronous with the timing of peak daylight duration. The PCA also revealed that indices were well associated with the five identified clusters, and that the clusters were best distinguished by the timing of the phenocycle<sub>A</sub> maximum rather than the amplitude, duration or modality (Supplementary Fig. 12).

We also found consistent linear relationships between the timing of the phenocycle<sub>A</sub> maximum and the average surface nitrate concentration (Fig. 4b). The timing of the phenocycle<sub>A</sub> maximum was positively related to the timing of peak daylight duration (insolation controlled) in locations where surface nitrate concentrations were highest. This relationship was consistent in the Atlantic ( $r = -0.7$ ;  $P < 0.0001$ ) and Indian ( $r = -0.73$ ;  $P < 0.0001$ ) Oceans, and was present but weaker in the Pacific Ocean ( $r = -0.49$ ;  $P < 0.0001$ ) where phytoplankton growth is also limited by iron availability<sup>26</sup> (Fig. 4b).

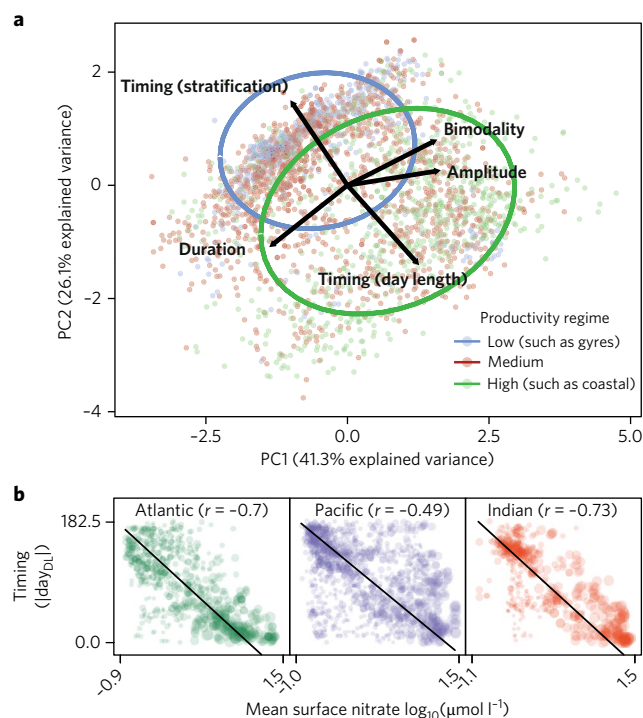


**Fig. 4 | Environmental correlates of phytoplankton phenology.** **a**, Principal component analysis describing the multivariate relationship among the main phenological indices. Colours depict the productivity regime: low (gyres; blue) and high (coastal and high latitude; green). PC1 and PC2 indicate principal components. **b**, The relationship between the average annual surface nitrate concentration and the timing of phenology in each cell, separated by ocean. The size of points depicts the absolute latitude of each cell; large points are high latitude, and small are low latitude. Lines are the model II ranged major axis regressions fitted to the data.

Globally, the phenocycle<sub>A</sub> amplitude was negatively related to average SST ( $r = -0.23$ ;  $P < 0.0001$ ; Supplementary Fig. 6). This relationship was strongest at high latitudes (>30° N:  $r = -0.44$ ; >30° S:  $r = -0.26$ ) but only weakly positive at low latitudes ( $r = 0.12$ ; Supplementary Fig. 6). We hypothesize that these relationships may be driven by metabolic effects, whereby warming waters accelerate heterotrophic production more rapidly than primary production<sup>38,39</sup>. This leads to increasing grazing pressure in warmer conditions, which could dampen high-amplitude peaks in phytoplankton biomass.

**Investigating causality.** We used multivariate structural equation models<sup>27,40</sup> (SEMs) to more fully explore the interplay of factors that structure the observed patterns of phytoplankton phenology. The models simultaneously estimated the effects of both physical (vertical mixing and insolation) and biological (grazing) processes on the phenocycle<sub>A</sub> within each cell, data permitting (Fig. 5a). SEMs were fitted to daily observations averaged from 1995 to 2015 (Supplementary Table 1). All variables were expressed in units of variance to enable interpretation of the SEM effects in common units, thus allowing quantification of relative importance. At high latitudes (>50° N and S), negative effects of increasing vertical mixing ( $\beta_{\text{VM}}$ ) on phenocycle<sub>A</sub> variability were observed, whereas positive effects were dominant in lower latitudes (<30° N and S; Fig. 5b and Supplementary Fig. 10). The effects of vertical mixing were particularly strong in the Indian Ocean, where monsoon dynamics are an important driver of phytoplankton productivity<sup>41</sup>. Positive effects of increasing insolation ( $\beta_{\text{I}}$ ) on phenocycles<sub>A</sub> were prevalent at high latitudes (Fig. 5c).

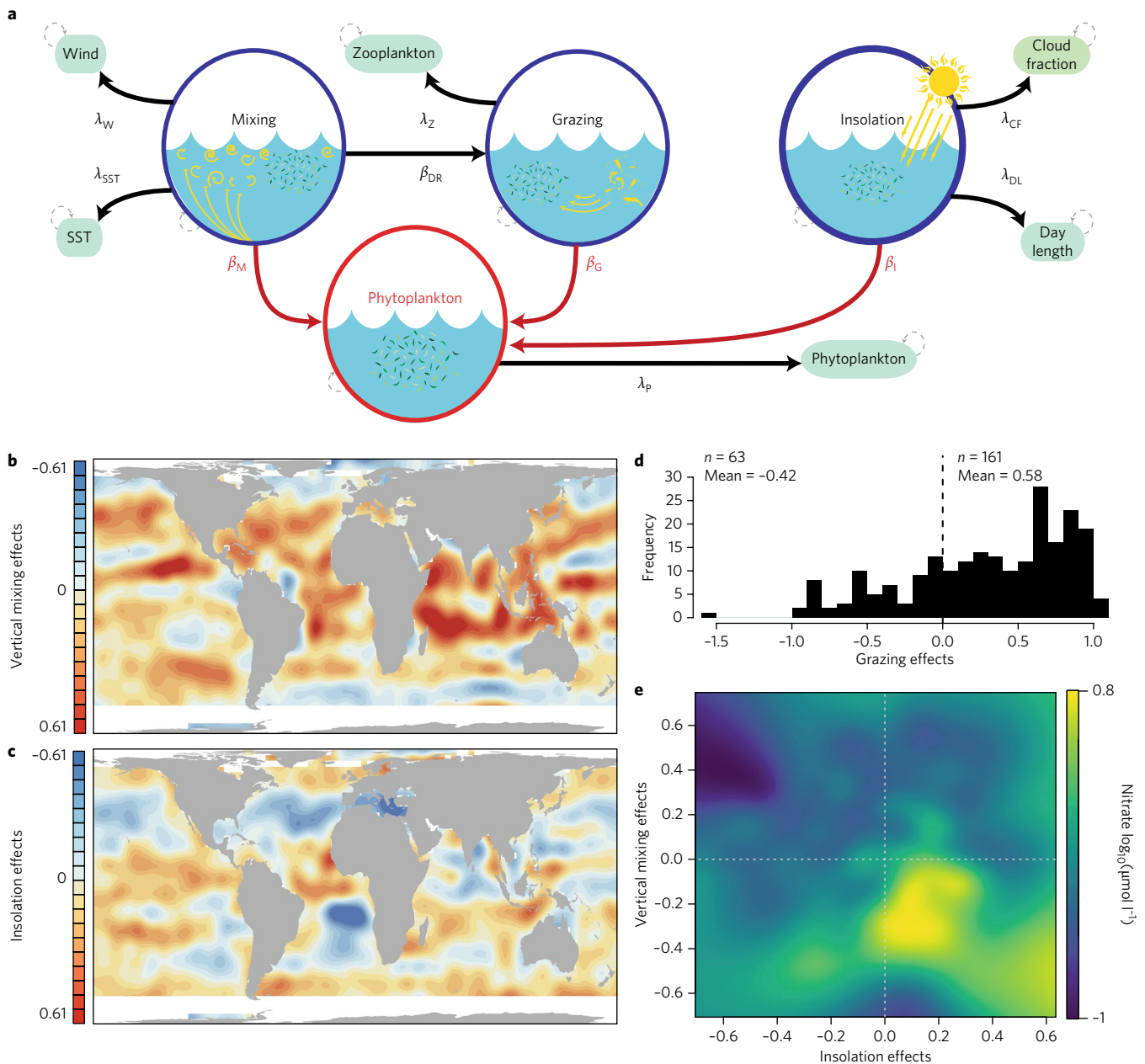


**Fig. 5 | Biotic and abiotic structuring of phytoplankton phenology.** **a**, The schematic depicts the structural equation model effects of environmental and biological processes on the phenocycles<sub>A</sub>. Observed variables are depicted as light green ellipses, and unobservable (latent) processes are depicted as larger circles. Single-headed arrows depict directed model relationships, and circular broken grey arrows depict variances. Unobservable effects of vertical mixing ( $\beta_M$ ), irradiance ( $\beta_I$ ), and grazing ( $\beta_G$ ), on phenocycles<sub>A</sub> are depicted in red, while effects of mixing on grazing via the dilution recoupling hypothesis<sup>81</sup> ( $\beta_{DR}$ ) are shown in black. **b, c**, Effects of vertical mixing  $\beta_M$  (**b**) and insolation  $\beta_I$  (**c**) on phenocycles<sub>A</sub> across the world's oceans. Colours depict the estimated effects within each grid cell. Dark blue denotes negative effects and dark red indicates positive effects. The values were spatially interpolated using a GAM (see Supplementary Information for mapped discrete values). **d**, Distribution of estimated effects of grazing  $\beta_G$  on phenocycles<sub>A</sub> (see Supplementary Fig. 14 for mapped grazing effects). **e**, Effects of vertical mixing and insolation on the phenocycles<sub>A</sub> as a function of average surface nitrate concentration in each grid cell. Colours depict the average surface nitrate concentration: dark blue depicts low values and yellow depicts high values. Dashed vertical and horizontal lines denote no effect of insolation and mixing processes, respectively.

Owing to incomplete data, evaluation of zooplankton grazing effects ( $\beta_G$ ) was limited to 224 (8%) of the 2,822 cells. Strong positive SEM interactions (mean: 0.58) between phytoplankton and zooplankton phenocycles, generally interpreted as evidence for resource control of grazers by phytoplankton<sup>42</sup>, were observed in most of the cells ( $72\% \pm 6\%$ ; Fig. 5d). Negative interactions, indicative of grazer control of phytoplankton, were weaker (mean:  $-0.42$ ) and less frequent globally ( $28\% \pm 5.5\%$ ), but were most frequent and

of greater magnitude at high latitudes ( $>50^\circ\text{N}$ ), and in cells in which surface nitrate was lowest and SST was highest (Supplementary Fig. 14). Interestingly, the effects of vertical mixing and insolation were weakly related ( $r^2 = 0.02$ ), but were well-connected through the average standing stock of surface nitrate ( $r^2 = 0.26$ ; Fig. 5e). In those grid cells where nitrate concentration was lowest (Fig. 5e, upper left quadrant), strong positive effects of vertical mixing and nutrient delivery, and strong negative effects of insolation, were observed.

These effects were opposite and of reduced magnitude in cells where average nitrate was highest (Fig. 5e, lower right quadrant).

SEM effects of vertical mixing and insolation were opposite in four of the five clusters, and grazing effects were positive in all clusters, with the magnitude declining from high (purple) to low (blue) latitude clusters (Supplementary Fig. 15). The yellow cluster was a notable outlier, showing large grazer effects and negative mixing and insolation effects, an atypical pattern that may be explained by its exceptionally even and broad (span: 165°) latitudinal distribution, relative to the other clusters (Fig. 2d).

**Marine versus terrestrial phenology patterns.** We evaluated the hypothesis that the seasonal development of primary producer biomass is similar on land and at sea. This objective was achieved by estimating terrestrial phenocycles, hereafter phenocycles<sub>NDVI</sub>, derived from the Normalized Difference Vegetation Index (Supplementary Table 1) using the statistical approach previously described for phytoplankton (equation (1) and Supplementary Fig. 1). Marine phenocycles<sub>A</sub> were virtually identical in the Northern and Southern Hemispheres and were fairly similar (median  $r=0.3$ ) to terrestrial phenocycles<sub>NDVI</sub> when compared across latitudes (Fig. 6a,b and Supplementary Fig. 17a). The strongest correlations ( $r>0.5$ ) occurred at mid-latitudes (20°–30°N and S) and in temperate mid- to high-latitudes (30°–70°N and S). The positive relationship between marine and terrestrial phenologies across extratropical latitudes may be driven by the effects of insolation on marine phenocycles<sub>A</sub> and by the strongly collinear effects of insolation and temperature on land phenocycles<sub>NDVI</sub>. Latitudinal patterns in the timing, amplitude and duration of marine and terrestrial phenocycles were also similar ( $r=0.26$  to  $0.3$ ; Fig. 6c).

Despite these broad similarities, differences were apparent at low latitudes (<10°N and S), where insolation does not limit primary production. There, phytoplankton growth is constrained by upwelling-nutrient delivery<sup>11,13</sup>, whereas the growth of terrestrial vegetation is primarily limited by precipitation<sup>43</sup>. Land-based anthropogenic activities may also obscure the correspondence between marine and terrestrial phenocycles. Modern agricultural practices have skewed natural vegetation phenologies by transforming native landscapes to optimize crop yield or value and regulating fertilizers, water and pesticides<sup>44</sup>.

Differences in the modality of terrestrial and marine phenology were also apparent across latitude ( $r=-0.14$ ; Fig. 6c) and globally. Globally, the proportion of bimodal phenocycles on land ( $61\% \pm 2.3\%$ ), was significantly greater than that observed in the oceans, ( $49.7\% \pm 1.8\%$ ), and of those reported in freshwater and estuarine systems ( $52\%$ )<sup>45</sup>. In contrast to terrestrial patterns, most bimodal phenocycles<sub>A</sub> in the ocean were observed at temperate mid-latitudes ( $64\% \pm 5\%$ ; 45°–65°N and S; Fig. 6c and Supplementary Fig. 5). This distinct marine latitudinal pattern may result from autumn storm activity which induces vertical mixing and surface nutrient delivery while insolation remains sufficient for photosynthesis. These latitudinal bands of bimodal phenocycles<sub>A</sub> may denote a transition zone between regimes primarily governed by insolation (high latitudes) and those governed by nutrient availability (low latitudes).

The overall similarity of terrestrial and marine phenologies suggests that insolation may act as a synchronizing driver of cyclic production globally, overriding the very different resource constraints of terrestrial versus marine vegetation at low latitudes.

## Discussion

We observed complex global patterns of marine phytoplankton phenology that varied strongly by latitude but were virtually identical in the Northern and Southern Hemispheres (median  $r=0.75$ ; range  $r=0.03$ – $0.99$ ). These spatial patterns were best distinguished along gradients of plankton productivity and productivity potential.

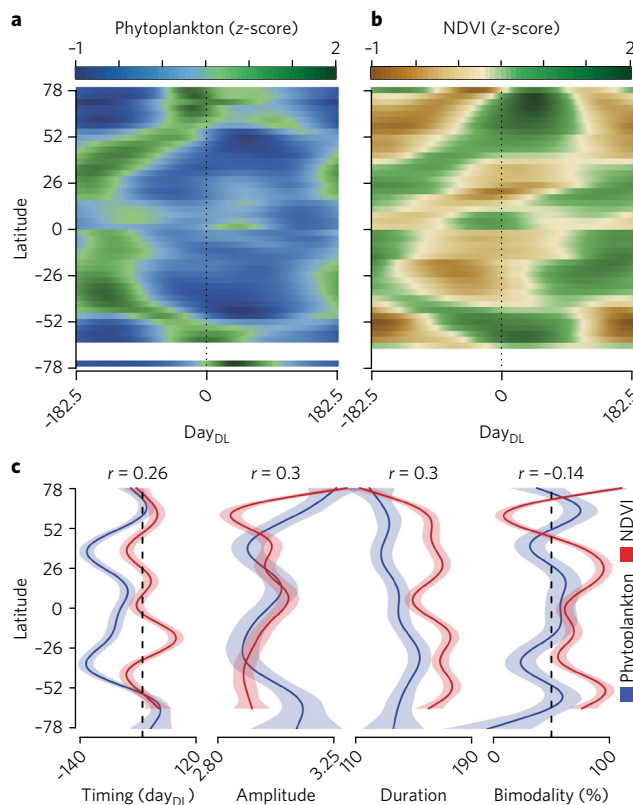


**Fig. 6 | Contrasting land and ocean phenology patterns.** **a, b**, Averaged phenocycles within each latitude band for **(a)** marine phytoplankton and **(b)** terrestrial vegetation from the NDVI. Colours depict the magnitude of the estimated phenocycles for each latitude in units of variance; for **(a)** dark green depicts high values and dark blue depicts low values, and for **(b)** dark green depicts high values and dark brown depicts low values. Phenocycles have been centred so that the peak duration of daylight hours is at 0. **(c)** Latitudinal trends in the average timing of maximum, amplitude, duration of maximum and proportion of bimodal phenocycles on land and at sea. Lines are best fits estimated from a GAM, and the shading depicts the 95% confidence interval. Blue represents marine and red represents terrestrial phenocycles.

In oligotrophic waters, particularly the vast oceanic gyres, phenologies were uniform over large geographical areas and were primarily driven by factors related to vertical mixing and nutrient delivery. In sharp contrast, phenologies in more productive, nutrient-replete waters were uniform over smaller geographic areas and were driven by factors related to insolation. These biogeographic patterns coincided with well-described oceanographic drivers of interannual phytoplankton biomass changes<sup>11,12</sup>. Zooplankton grazer phenology was more commonly driven by phytoplankton phenology than vice versa and was best related to nutrient availability and temperature, consistent with mesocosm studies<sup>38,39</sup>.

Until now, global analyses of phytoplankton phenology have primarily used data from a single source (satellite remote sensing) to describe empirical patterns<sup>22,23</sup>. The analysis framework that we have developed robustly integrates observations from a more diverse and ever-changing suite of phytoplankton observation platforms<sup>13</sup>, eliminating reliance on single sensors and increasing the spatial and temporal scale of inquiry. Consequently, our findings are a new first approximation of the effects of environmental variability on marine phytoplankton phenology. Such comprehensive approaches are pivotal to understanding and anticipating the potential impacts of ongoing environmental changes<sup>11,12,15,24,37</sup> on marine ecosystems. Future studies of this data set could include more complex interactions such as biologically mediated nitrogen fixation<sup>46</sup>, wind-driven

iron deposition<sup>47</sup>, nutrient co-limitation<sup>26</sup> or size-based grazing<sup>42</sup>. Likewise, the focus could be expanded beyond aggregate biomass to consider the dynamics of individual species, functional groups or size classes, all of which may exhibit distinct phenological dynamics.

Our analyses indicated that the common assumption of basin-scale uniformity of phytoplankton phenology is invalid in eight of the ten large ocean regions examined. This finding has important practical implications for observational time-series analyses and predictive ocean modelling, which have often assumed that phenology is uniform at large spatial scales<sup>10,11,36,37</sup>.

Our analyses also revealed that patterns of vegetative phenology at land and sea are broadly similar globally (median  $r=0.3$ ). Differences were apparent at low latitudes and may be driven by differential resource requirements such as water on land<sup>28</sup> and vertical mixing in the oceans<sup>11,13</sup>. Variability in the relationship may also be driven by modern agricultural practices, which have disproportionately altered the seasonal cycles of terrestrial primary producers<sup>44</sup>. Another important difference is the rapid turnover time of primary producer biomass in the oceans (average 2 to 6 days)<sup>18</sup>, which is over 1,000 times faster than on land (average 19 years)<sup>48</sup>, creating a more rapid phenological response to environmental variation in the oceans. These differences notwithstanding, the overarching similarity of marine and terrestrial phenocycles suggests that they are governed by common underlying dynamics<sup>49</sup> and points to a paramount effect of insolation. This finding calls for improved communication and collaboration between terrestrial and marine ecologists in the search for a unified understanding of global macroecological change<sup>49</sup>.

## Methods

**Data.** *Phytoplankton data.* Historically, phytoplankton carbon (C) biomass has been inferred from total chlorophyll pigment concentration (Chl), upper-ocean transparency using the standardized Secchi disk<sup>50,51</sup>, semi-quantitative ocean colour measurements using the continuous plankton recorder<sup>52</sup> (CPR) or Forel–Ule scale<sup>53</sup>, and other metrics<sup>54</sup>. The ability of these indices to reliably assess phytoplankton C biomass has been debated<sup>55,56</sup>. Rather than relying on a single indicator of biomass, we compiled measurements of these variables from all available sources from 1995 to 2015 (see Supplementary Information and Supplementary Table 1 for details). Chlorophyll values were derived from shipboard *in situ* sampling approaches such as spectrophotometric and fluorometric analyses of filtered seawater residues, as well as from *in vivo* measurements of phytoplankton fluorescence<sup>57</sup>, calibrated measurements of upper-ocean transparency or colour<sup>58</sup>, and from satellite-derived upper-ocean-leaving radiances<sup>59,60</sup>. Phytoplankton colour index (PCI) measurements from the Continuous Plankton Recorder program (CPR) were obtained in the North Atlantic Ocean.

To minimize sampling effects associated with the optical complexities of nearshore waters, any observations located within 1 km from any coastline, or in waters less than 10 m deep, were removed from the database. The observations in the database are reflective of phytoplankton concentrations within about the upper 20 m of the oceans, where the vast majority of oceanic primary production occurs. See Supplementary Table 1 for additional details of the phytoplankton database.

**Zooplankton data.** Standardized measurements of zooplankton abundance are difficult to obtain. Zooplankton has been sampled using a range of approaches and instrumentation, and have been reported in units of dry weight, wet weight or species counts<sup>61,62</sup>. Rather than relying on a single indicator of zooplankton abundance, we compiled measurements of these variables from all available sources (Supplementary Table 1). Counts of individual zooplankton species were obtained from the CPR programme operating in the northwest Atlantic Ocean, the North Pacific Ocean, the Southern Ocean, and in the waters surrounding Australia<sup>63</sup>. To reduce bias associated with different levels of species identification and size between survey programmes, we retained observations for copepod species only. Measurements of total mesozooplankton biomass were obtained from the COPEPOD global plankton database<sup>64</sup>. The database represents the accumulation of 153,163 observations from 30 institutions standardized to common units of 200 m depth-integrated carbon biomass.

**Terrestrial vegetation data.** Measurements of the noise-reduced NDVI were obtained from the Advanced Very High-Resolution Radiometer Vegetation Health Indices Product (AVHRR-VHP). The observations were extracted from the National Oceans and Atmospheric Administration Center for Satellite Applications and Research (NOAA STAR) programme as weekly observations on a global 16-km grid (Supplementary Table 1).

**Environmental data.** Sea surface temperature (0–20 m; SST; °C) and neutral surface wind speed (at 10 m;  $m s^{-1}$ ) observations were obtained from the NOAA AVHRR Pathfinder Version 5.2 (PFV5.2), acquired from the US National Oceanographic Data Center and the Group for High Resolution Sea Surface Temperature. The PFV5.2 data are an updated version of the Pathfinder Version 5.0 and 5.1 collections described in ref. <sup>65</sup>. Surface (0–20 m) nitrate concentration ( $\mu mol l^{-1}$ ) data were obtained from the NOAA World Ocean Atlas V.2. Fractional cloud cover estimates were obtained from the NASA Earth Observatory database, derived from observations by the MODIS instrument. A stratification index was calculated from subsurface ocean profiles of temperature and salinity extracted from Hadley EN3 data<sup>66</sup> (1950–2015). Stratification was calculated as the density difference between the surface and 100 m (refs <sup>64,65</sup>). The initial temperature and density values were chosen at a depth of 5 m to eliminate any bias in the profile due to ‘skin effects’ at the ocean surface<sup>66</sup>. A bivariate linear interpolation approach was used to calculate the exact values at 5 and 100 m.

The bathymetry associated with each observation and grid cell was calculated from global gridded bathymetry data (30-arcsecond resolution), acquired from the General Bathymetric Chart of the Oceans database (GEBCO 08). The distance from the nearest coastline was calculated from the Global Self-consistent Hierarchical High-resolution Shoreline Database (GSHHS v1.10).

**Analyses.** *Phenology estimation.* The phytoplankton database was divided into equal-area grid cells and into data categories (see Supplementary Table 1). Observations were projected onto a global equal-area grid of 48 rows by 88 columns, equivalent to 2.4° latitude by 4° longitude spacing at the Equator. Because these indices of phytoplankton biomass were infrequently coincident in space and time, standardization by intercalibration was impossible. Instead, the observations were treated independently as five distinct categories, which were identified according to the measurement units, observation platform and inter-comparability (Supplementary Table 1). Based on the strong estimated ( $r=0.98$ ) and reported<sup>23</sup> agreement between SeaWiFS and MODIS Chl observations, we calculated the average Chl values and treated them as a single data type. For each unique combination of the equal-area grid cell (G), and data category (D), a single cyclic intra-annual trend in phytoplankton concentration was estimated, hereafter referred to as a phenocycle<sub>G,D</sub>. The phenocycles<sub>G,D</sub> were estimated using GAMs, which are a flexible class of statistical models capable of estimating the response as a discrete, monotonic, non-monotonic, cyclic function of the covariates<sup>67</sup>. The GAM approach is well suited because it enables estimation of each phenocycle<sub>G,D</sub> as a cyclical function of intra-annual variability (day) while accounting for any inter-annual variability (annual time trend), interpolating over missing observations and quantifying the uncertainty in the predicted phenocycle<sub>G,D</sub><sup>10,11</sup>. The phenocycles<sub>G,D</sub> were estimated as:

$$\hat{\mu}_i = \beta_0 + f_1(\text{day}_i) + \beta_1 \text{year}_i + \varepsilon_i \quad (1)$$

where  $i$  are the individual observations,  $\hat{\mu}_i$  is the expected mean phytoplankton concentration,  $\text{day}_i$  and  $\text{year}_i$  are the day of the year and year,  $\beta_0$  is the model intercept,  $\beta_1$  denotes a discrete parametric effect and  $f_1$  denotes the functional effect estimated from the data, and  $\varepsilon_i$  represents the residual error term. The functional effect in the model allows a phenocycle<sub>G,D</sub> to be estimated as a continuous, cyclic smooth curve. Importantly, the model allows a distinct phenology to be estimated within each year, while accounting for any time-dependent variability in phytoplankton concentration occurring between years. Before model fitting, the day of the year in each grid cell and data type was iteratively adjusted to ensure that observations were present at both the start and end of the phenocycle<sub>G,D</sub>. This procedure was necessary to ensure that the model was interpolating over missing observations, rather than extrapolating beyond them, and to satisfy the assumptions of the cyclic spline used in phenocycle<sub>G,D</sub> estimation. The residual variability in the GAMs was examined to verify statistical assumptions of normality, independence, homogeneity of variance, and linearity. Following phenocycle<sub>G,D</sub> estimation, the day of the year values were re-transformed to their original scale. The units of the phenocycles<sub>G,D</sub> were standardized by converting the predicted values to standard deviations from the mean ( $z$ -score) as

$$z_{G,D,i} = \frac{x_{G,D,i} - \mu_{G,D}}{\sigma_{G,D}} \quad (2)$$

where  $x_{G,D,i}$  is the predicted value of the phenocycle<sub>G,D</sub> on day  $i$ ,  $\mu_{G,D}$  is the mean, and  $\sigma_{G,D}$  is the standard deviation of the predicted phenocycle<sub>G,D</sub>.

**Data sufficiency criteria.** We quantitatively identified how many measurements were required to accurately resolve phenological variability through simulation analyses. Three phenocycles were simulated to approximate those possible in the ocean in terms of modality, amplitude and periodicity<sup>11,21,23</sup> (see Supplementary Information for details). To these simulated phenocycles, we added two levels of Gaussian-distributed white noise with mean set to 0, and variances set to 100% or 300% of the upper 99th percentile of all phenocycle<sub>G,D</sub> variances estimated using global field observations (Supplementary Figs. 2 and 3). Each simulated phenocycle was subsampled to obtain sample sizes ranging from 6 to 75 in increments of 1, with 100 replicates each. For each subsample ( $n=6,900$ ), the ability of our GAM

approach to correctly recover the ‘true’ phenocycle was assessed. We observed that long stretches of missing observations had the strongest univariate effect on the ability of our approach to recover the true phenocycle, but that the number of available months of observations was also important (Supplementary Figs. 2 and 3). The true phenocycle was more accurately recovered if it was unimodal and the variance was low. Cumulatively, our simulation analysis suggested that a minimum of 8 months of observations, with no more than 75 consecutive missing days, was required to recover the ‘true’ phenocycle accurately. At these levels, the average probability of correct phenocycle classification was 94% ( $\pm 6\%$ ), and the average correlation between the recovered and true phenocycle was 0.97 ( $\pm 0.06$ ).

In high-latitude grid cells where insolation and ice cover significantly limit phytoplankton sampling, long stretches of consecutive missing observations and months are commonplace. These often correspond to situations in which phytoplankton concentrations are extremely low. In these instances, data sufficiency was defined using only those observations available during the months when insolation and ice cover were not limiting. This criteria was defined as months where the average duration of insolation was  $>2$  hours and where average ice cover was  $<75\%$ . For the remaining part of the series, data sufficiency was defined as instances where the number of months containing observations was equal to the number of months where growth was not limited by insolation or ice minus one, where at least 6 months of observations were available.

**Multi-model averaging.** In grid cells containing more than one data type, standardized phenocycles<sub>G,D</sub> were integrated using multi-model averaging<sup>25</sup>. Multi-model inference aids in ranking and integration of an ensemble set of plausible phenocycles<sub>G,D</sub> using information theory, thereby incorporating the uncertainty of the individual predictions<sup>10,25,68</sup>. The weighting is usually based on the Akaike Information Criterion (AIC), which helps to optimize model fit and complexity<sup>25</sup>. The AIC is calculated as

$$AIC = -2\ln\left[L(\hat{\theta}_p | y)\right] + 2p \tag{3}$$

where  $L(\hat{\theta}_p | y)$  is the maximum likelihood estimate of the model (that is, the goodness of fit), and  $p$  is the number of estimable parameters in the model (that is, the complexity). However, in our situation, the model complexity is invariant, and ensemble averaging was therefore based on the model goodness of fit, which for GAMs is the proportion of deviance explained<sup>67</sup>. By eliminating the reliance on a single model, the robustness of the model inference is improved in much the same way as ensemble forecasts do for meteorological or climate projections. Normalized multi-model weights for each ensemble model ( $w_m$ ) are calculated as

$$w_m = \frac{\exp\left(-\frac{1}{2\Delta_m}\right)}{\sum_{m=1}^R \exp\left(-\frac{1}{2\Delta_m}\right)} \tag{4}$$

where  $R$  represents the total number of models fitted, and

$$\Delta_m = AIC_m - AIC_{\min} \tag{5}$$

where  $AIC_m$  is the AIC score for model  $m$ , and  $AIC_{\min}$  is the minimum AIC (top-ranking) score across the ensemble of models. This approach favours the model containing the largest amount of ‘information’<sup>25,69</sup>. The multi-model averaged predictions were then derived as

$$\bar{\theta}_i = \sum_{m=1}^R w_m \hat{\theta}_{i,m} \tag{6}$$

where  $\bar{\theta}_i$  is the multi-model averaged prediction on day  $i$ ,  $\hat{\theta}_{i,m}$  is the prediction from model  $m$  on day  $i$ , and  $w_m$  is the standardized weight for model  $m$ . The multi-model importance was calculated as  $\sum \Delta_m$  for each model containing the predictor, and therefore ranges between 0 and 1. Through this procedure, we estimated a single standardized, multi-model ensemble-averaged phenocycle, or phenocycle<sub>A</sub>, for each individual grid cell averaged between 1995 and 2015.

Zooplankton phenocycles used in causal modelling (described below) were estimated using the statistical procedures outlined above.

**Fuzzy clustering.** Fuzzy clustering was used to characterize the degree of similarity between the phenocycles<sub>A</sub><sup>32</sup>. Fuzzy clustering operates through the assignment of probabilities of cluster membership and thus allows the relative certainty of cluster identity to be quantified. The objective of the fuzzy clustering algorithm is to minimize the objective function

$$\sum_{c=1}^k \frac{\sum_{i=1}^n \sum_{j=1}^n u_{ic}^r u_{jc}^r d(i,j)}{2 \sum_{j=1}^n u_{jc}^r} \tag{7}$$

where  $n$  is the number of phenocycles<sub>A</sub>,  $k$  is the cluster dimension,  $r$  is the membership exponent (set to 2),  $d(i,j)$  is the dissimilarity between phenocycles<sub>A</sub>

$i$  and  $j$ , and  $u_{ic}^r$  and  $u_{jc}^r$  are the memberships of phenocycles<sub>A</sub>  $i$  and  $j$  to cluster  $c$ . Choice of  $k$  was based on iterative substitution;  $k=5$  was the largest number possible while still maintaining a sufficient degree of cluster separation and relatively high silhouette values within clusters. The clustering was applied to phenocycles<sub>A</sub> from all locations in the database. We used  $1-r$  as the estimate of  $d(i,j)$ , where  $r$  is the Pearson correlation between phenocycles<sub>A</sub>  $i$  and  $j$ . For each phenocycle<sub>A</sub>, a silhouette statistic ( $S_j$ ) was calculated that quantified how well each phenocycle<sub>A</sub> was defined by its cluster. Silhouette values were derived as

$$S_j = \frac{b(j) - a(j)}{\max\{a(j), b(j)\}} \tag{8}$$

where  $a(j)$  is the average dissimilarity between phenocycle<sub>A</sub>  $j$  within cluster  $c$  and all other phenocycles<sub>A</sub> within cluster  $c$ , and  $b(j)$  is the minimum of all dissimilarities between phenocycle<sub>A</sub> and all phenocycles<sub>A</sub> not in  $c$ . Phenocycles<sub>A</sub> with large silhouette values are very well clustered, and small values denote poor clustering.

**Indices of phenology.** The specific attributes of phytoplankton phenology were quantified by calculating second-order indices from the phenocycles<sub>A</sub>: (1) the timing of the seasonal maximum, (2) the relative duration of the period of maximum abundance, (3) the amplitude of the phenocycles<sub>A</sub> and (4) the modality of the phenocycles<sub>A</sub> (Fig. 1c). The timing was the day when the maximum phenocycle<sub>A</sub> occurred. The duration of the period of maximum growth was calculated relative to the timing of the maximum and the point at which the phenocycle<sub>A</sub> decayed to 0 (the mean). The initiation and termination were the days when the phenocycle<sub>A</sub> decayed from its seasonal maximum to 0. The duration was the number of days between the initiation and termination. The amplitude was the total range (maximum – minimum) of each standardized phenocycle<sub>A</sub>. The modality of each phenocycle<sub>A</sub> was estimated by calculating Hartigan’s dip test for unimodality<sup>70</sup>.

**Distance decorrelation scales.** To estimate the spatial scales over which the phenocycles<sub>A</sub> were coherent, a distance decorrelation scale was estimated for each grid cell. Informed by approaches developed elsewhere<sup>71,72</sup>, the decorrelation scale was estimated as the omnidirectional distance at which the correlation between phenocycles<sub>A</sub> decayed to  $e^{-1}$ . The exact distance was estimated using GAMs that were capable of flexibly approximating the range of decay forms within each grid cell. As a sensitivity check, decorrelation scales were also estimated using an exponential decay model (see Supplementary Information for details; Supplementary Fig. 7). Although these approaches produced similar results ( $r=0.64$ ), decorrelation distances estimated with the exponential decay model were more sensitive to correlations at long distances and the model assumptions were violated in many grid cells. We also evaluated the symmetry and directionality of phytoplankton phenology decorrelation. Decorrelation was estimated along strictly zonal and meridional axes (Supplementary Fig. 9), as well as in the four cardinal directions (Supplementary Fig. 10). In many cells, decorrelation scales estimated in strictly longitudinal directions did not decay to  $e^{-1}$  and were set to the maximum empirically derived scale (8,000 km). Because the decorrelation scales were estimated omnidirectionally, the areal extent of phenocycle<sub>A</sub> decorrelation ( $\text{km}^2$ ) was also estimated as  $\pi r^2$ , where  $r$  is the estimated spatial decorrelation distance (km).

**Causal modelling.** To statistically quantify and partition the causal effects of mixing, insolation and grazing on marine phytoplankton phenology patterns, we used SEMs<sup>27</sup>. These are estimated as a network of interacting linear models within which variables can function as both predictors and/or responses, and within which relationships between unobservable (latent) processes of interest can be estimated. SEMs are widely used to investigate complex causal networks in social sciences and are increasingly used in ecology<sup>73,74</sup>. They are valuable tools for distinguishing between processes that are of interest but cannot be directly measured or observed (latent constructs; Fig. 5a circles; denoted  $\beta$ ) from measurements that are useful but imperfect proxies for these processes (observed variables; Fig. 5a ellipses; denoted  $\lambda$ ). Resolving complex interactions and identifying causality is one of the important challenges in ecological research<sup>75</sup>. Although the SEMs are not a panacea and are not ideally suited to estimating interacting and nonlinear effects, they can be used to develop a more rigorous and robust causal inference network than can be achieved with traditional linear model or correlative approaches<sup>76</sup>. For each grid cell for which data permitted, we fitted a SEM to estimate the influence of processes related to vertical mixing (wind speed and SST), insolation (daylight hours and cloud cover fraction) and grazing (zooplankton abundance) on the phytoplankton phenocycles<sub>A</sub> (Fig. 5a). Possible effects of vertical mixing on grazing (for example ref. <sup>77</sup>) were also incorporated. All SEM effects were estimated from daily observations. Vertical mixing processes were derived from daily observations of SST and surface wind speed, while insolation processes were derived from daily observations of daylight hours and cloud fractional cover. All SEM effects were estimated within the linear models using maximum likelihood and the Lavaan package<sup>78</sup> in the R statistical computing platform<sup>79</sup>; technical and philosophical underpinnings of SEMs may be found elsewhere<sup>40,76,80</sup>.

**Data availability.** All of the data sets used in this study are publicly available through the links provided in Supplementary Table 1.

Received: 23 February 2017; Accepted: 18 July 2017;

Published online: 04 September 2017

## References

- Randerson, J. T., Field, C. B., Fung, I. Y. & Tans, P. P. Increases in early season ecosystem uptake explain recent changes in the seasonal cycle of atmospheric CO<sub>2</sub> at high northern latitudes. *Geophys. Res. Lett.* **26**, 2765–2768 (1999).
- Boyd, P. W. & Newton, P. P. Evidence of the potential influence of planktonic community structure on the interannual variability of particulate carbon flux. *Deep Sea Res. Part I* **42**, 619–639 (1995).
- Eviner, V. T., Chapin, F. S., Vaughn, C. E., Chapin, F. S. III & Vaughn, C. E. Seasonal variations in plant species effects on soil N and P dynamics. *Ecology* **87**, 974–986 (2006).
- Inouye, D. W., Barr, B., Armitage, K. B. & Inouye, B. D. Climate change is affecting altitudinal migrants and hibernating species. *Proc. Natl Acad. Sci. USA* **97**, 5–8 (2000).
- Post, E. et al. Climate change reduces reproductive success of an Arctic herbivore through trophic mismatch. *Phil. Trans. R. Soc. Lond. B. Biol. Sci.* **363**, 2369–2375 (2008).
- Platt, T., Fuentes-Yaco, C. & Frank, K. T. Spring algal bloom and larval fish survival. *Nature* **423**, 398–399 (2003).
- Rathcke, B. & Lacey, E. P. Phenological patterns of terrestrial plants. *Annu. Rev. Ecol. Syst.* **16**, 179–214 (1985).
- Worm, B. et al. Impacts of biodiversity loss on ocean ecosystem services. *Science* **314**, 787–90 (2006).
- Vantrepotte, V. & Mélin, F. Inter-annual variations in the SeaWiFS global chlorophyll *a* concentration (1997–2007). *Deep Sea Res. Part I* **58**, 429–441 (2011).
- Boyce, D. G., Dowd, M., Lewis, M. R. & Worm, B. Estimating global chlorophyll changes over the past century. *Prog. Oceanogr.* **122**, 163–173 (2014).
- Boyce, D. G., Lewis, M. R. & Worm, B. Global phytoplankton decline over the past century. *Nature* **466**, 591–596 (2010).
- Gregg, W. W., Conkright, M. E., Ginoux, P., O'Reilly, J. E. & Casey, N. W. Ocean primary production and climate: global decadal changes. *Geophys. Res. Lett.* **30**, 1809 (2003).
- Boyce, D. G. & Worm, B. Patterns and ecological implications of historical marine phytoplankton change. *Mar. Ecol. Prog. Ser.* **534**, 251–272 (2015).
- Buitenwerf, R., Rose, L. & Higgins, S. I. Three decades of multi-dimensional change in global leaf phenology. *Nat. Clim. Change* **5**, 364–368 (2015).
- Fu, Y. H. et al. Declining global warming effects on the phenology of spring leaf unfolding. *Nature* **526**, 104–107 (2015).
- Fridley, J. D. Extended leaf phenology and the autumn niche in deciduous forest invasions. *Nature* **485**, 359–362 (2012).
- Field, C. B., Behrenfeld, M. J. & Randerson, J. T. Primary production of the biosphere: integrating terrestrial and oceanic components. *Science* **281**, 237–240 (1998).
- Falkowski, P. & Ravens, J. A. *Aquatic Photosynthesis* (Blackwell Science, 1997).
- Benincà, E. et al. Chaos in a long-term experiment with a plankton community. *Nature* **451**, 822–825 (2008).
- Demarcq, H., Reygondeau, G., Alvain, S. & Vantrepotte, V. Monitoring marine phytoplankton seasonality from space. *Remote Sens. Environ.* **117**, 211–222 (2012).
- Racault, M. F., Le Quéré, C., Buitenhuis, E., Sathyendranath, S. & Platt, T. Phytoplankton phenology in the global ocean. *Ecol. Indic.* **14**, 152–163 (2012).
- D'Ortenzio, F., Antoine, D., Martinez, E. & Ribera d'Alcalà, M. Phenological changes of oceanic phytoplankton in the 1980s and 2000s as revealed by remotely sensed ocean-color observations. *Global Biogeochem. Cycles* **26**, 1–16 (2012).
- Sapiano, M. R. P., Brown, C. W., Schollaert Uz, S. & Vargas, M. Establishing a global climatology of marine phytoplankton phenological characteristics. *J. Geophys. Res. Ocean* **117**, 1–16 (2012).
- Morán, X. A. G. et al. Increasing importance of small phytoplankton in a warmer ocean. *Global Change Biol* **16**, 1137–1144 (2010).
- Burnham, K. P. & Anderson, D. R. *Model Selection and Multi-Model Inference: A Practical Information-Theoretic Approach* (Springer, 2002).
- Moore, C. M. et al. Processes and patterns of oceanic nutrient limitation. *Nat. Geosci.* **6**, 1–10 (2013).
- Wright, S. S. Correlation and causation. *J. Agric. Res* **20**, 557–585 (1921).
- Schimel, D. S. et al. Climate and nitrogen controls on the geography and timescales of terrestrial biogeochemical cycling. *Global Biogeochem. Cycles* **10**, 677 (1996).
- Hastie, T. & Tibshirani, R. Generalized additive models. *Stat. Sci.* **1**, 297–318 (1986).
- Vargas, M., Brown, C. W. & Sapiano, M. R. P. Phenology of marine phytoplankton from satellite ocean color measurements. *Geophys. Res. Lett.* **36**, 2–6 (2009).
- Behrenfeld, M. J. et al. Annual boom–bust cycles of polar phytoplankton biomass revealed by space-based lidar. *Nat. Geosci.* **10**, 118–122 (2017).
- Kaufman, L. & Rousseeuw, P. J. *Finding Groups in Data: An Introduction to Cluster Analysis* (Wiley, 1990).
- Sournia, A. Cycle annuel du phytoplancton et de la production primaire dans les mers tropicales. *Mar. Biol.* **3**, 287–303 (1969).
- Longhurst, A. Seasonal cooling and blooming in tropical oceans. *Deep Sea Res. Part I* **40**, 2145–2165 (1993).
- Lumpkin, R. & Johnson, G. C. Global ocean surface velocities from drifters: mean, variance, El Niño–Southern Oscillation response, and seasonal cycle. *J. Geophys. Res.* **118**, 2922–3006 (2013).
- Behrenfeld, M. J., Boss, E., Siegel, D. A. & Shea, D. M. Carbon-based ocean productivity and phytoplankton physiology from space. *Global Biogeochem. Cycles* **19**, 1–14 (2005).
- Falkowski, P. G. & Wilson, C. Phytoplankton productivity in the North Pacific ocean since 1900 and implications for absorption of anthropogenic CO<sub>2</sub>. *Nature* **358**, 741–743 (1992).
- Lewandowska, A. M. et al. Effects of sea surface warming on marine plankton. *Ecol. Lett.* **17**, 614–623 (2014).
- O'Connor, M. I., Piehler, M. F., Leech, D. M., Anton, A. & Bruno, J. F. Warming and resource availability shift food web structure and metabolism. *PLoS Biol.* **7**, 1–6 (2009).
- Grace, J. B. *Structural Equation Modeling in Natural Systems* (Cambridge Univ. Press, 2006).
- Marra, J. & Moore, T. S. Monsoons, islands, and eddies: their effects on phytoplankton in the Indian Ocean. *Geophys. Monogr. Ser.* **185**, 57–70 (2009).
- Boyce, D. G., Frank, K. T. & Leggett, W. C. From mice to elephants: overturning the 'one size fits all' paradigm in marine plankton food chains. *Ecol. Lett.* **18**, 504–515 (2015).
- Reich, P. B. Phenology of tropical forests: patterns, causes, and consequences. *Can. J. Bot.* **73**, 164–174 (1995).
- Menzel, A., von Vopelius, J., Estrella, N., Schleip, C. & Dose, V. Farmers' annual activities are not tracking the speed of climate change. *Clim. Res* **32**, 201–207 (2006).
- Winder, M. & Cloern, J. E. The annual cycles of phytoplankton biomass. *Phil. Trans. R. Soc. Lond. B Biol. Sci.* **365**, 3215–3226 (2010).
- Capone, D. G., Zehr, J. P., Paerl, H. W., Bergman, B. & Carpenter, E. J. Trichodesmium, a globally significant marine cyanobacterium. *Science* **276**, 1221–1229 (1997).
- Jickells, T. D. et al. Global iron connections between desert dust, ocean biogeochemistry, and climate. *Science* **308**, 67–71 (2005).
- Russel, G., Jarvis, P. G. & Monteith, J. L. *Plant Canopies: Their Growth, Form and Function* (Cambridge Univ. Press, 1989).
- Webb, T. J. Marine and terrestrial ecology: unifying concepts, revealing differences. *Trends Ecol. Evol.* **27**, 535–541 (2012).
- Tyler, J. E. The Secchi disk. *Limnol. Oceanogr.* **13**, 1–6 (1968).
- Collier, A., Finlayson, G. M. & Cake, E. W. On the transparency of the sea. *Limnol. Oceanogr.* **13**, 391–394 (1968).
- Batten, S. D. et al. CPR sampling: the technical background, materials and methods, consistency and comparability. *Prog. Oceanogr.* **58**, 193–215 (2003).
- Forel, F. A. Une nouvelle forme de la gamme de couleur pour l'étude de l'eau des lacs. *Arch. Sci. Phys. Nat. Phys./Soc. Phys. d'Hist. Nat. Genève* **6** (1890).
- Harvey, H. W. Measurement of phytoplankton population. *J. Mar. Biol. Assoc. UK* **19**, 761–73 (1934).
- Geider, R. J. Light and temperature-dependence of the carbon to chlorophyll-*a* ratio in microalgae and cyanobacteria — implications for physiology and growth of phytoplankton. *New Phytol.* **106**, 1–34 (1987).
- Behrenfeld, M. J. et al. Reevaluating ocean warming impacts on global phytoplankton. *Nat. Clim. Change* **6**, 1–27 (2015).
- Jeffrey, S. W., Mantoura, R. F. C. & Wright, S. W. *Phytoplankton Pigments in Oceanography*. Monographs on Oceanographic Methodology **10** (UNESCO, 1997).
- Boyce, D. G. D. G., Lewis, M. & Worm, B. Integrating global chlorophyll data from 1890 to 2010. *Limnol. Oceanogr. Methods* **10**, 840–852 (2012).
- Hovis, W. A. et al. Nimbus-7 coastal zone color scanner: system description and initial imagery. *Science* **210**, 60–63 (1980).
- McClain, C. R., Feldman, G. C. & Hooker, S. B. An overview of the SeaWiFS project and strategies for producing a climate research quality global ocean bio-optical time series. *Deep Sea Res. II* **51**, 5–42 (2004).
- Moriarty, R. & O'Brien, T. D. Distribution of mesozooplankton biomass in the global ocean. *Earth Syst. Sci. Data* **5**, 45–55 (2013).
- Casey, K. S., Brandon, T. B. & Cornillon, P. in *Oceanography from Space: Revisited* 1–375 (Springer, 2010).

63. Ingleby, B. & Huddleston, M. Quality control of ocean temperature and salinity profiles — historical and real-time data. *J. Mar. Syst.* **65**, 158–175 (2007).
64. Li, W. K. W. Macroecological patterns of phytoplankton in the northwestern North Atlantic Ocean. *Nature* **419**, 154–157 (2002).
65. Behrenfeld, M. J. et al. Climate-driven trends in contemporary ocean productivity. *Nature* **444**, 752–755 (2006).
66. Fairall, C. W. et al. Cool-skin and warm-layer effects on sea surface temperature. *Geophys. Res. Lett.* **101**, 1295–1308 (1996).
67. Wood, S. N. *Generalized Additive Models: An Introduction with R* (Chapman & Hall/CRC, 2006).
68. Johnson, J. B. & Omland, K. S. Model selection in ecology and evolution. *Trends Ecol. Evol.* **19**, 101–108 (2004).
69. Burnham, K. P. & Anderson, R. P. Multimodel inference: understanding AIC and BIC in model selection. *Sociol. Methods Res.* **33**, 261–304 (2004).
70. Hartigan, J. A. & Hartigan, P. M. The dip test of unimodality. *Ann. Stat.* **13**, 70–84 (1985).
71. Myers, R. A., Mertz, G. & Bridson, J. M. Spatial scales of interannual recruitment variations of marine, anadromous, and freshwater fish. *Can. J. Fish. Aquat. Sci.* **54**, 1400–1407 (1997).
72. Frank, K. T., Petrie, B., Leggett, W. C. & Boyce, D. G. Large scale, synchronous variability of marine fish populations driven by commercial exploitation. *Proc. Natl Acad. Sci. USA* **113**, 8248–8253 (2016).
73. Duffy, J. E. et al. Biodiversity mediates top-down control in eelgrass ecosystems: a global comparative-experimental approach. *Ecol. Lett.* **18**, 696–705 (2015).
74. Mora, C. et al. Global human footprint on the linkage between biodiversity and ecosystem functioning in reef fishes. *PLoS Biol.* **9**, e1000606 (2011).
75. Sugihara, G. et al. Detecting causality in complex ecosystems. *Science* **338**, 496–500 (2012).
76. Pearl, J. Causal inference in statistics: an overview. *Stat. Surv.* **3**, 96–146 (2009).
77. Behrenfeld, M. J. Abandoning Sverdrup's critical depth hypothesis on phytoplankton blooms. *Ecology* **91**, 977–89 (2010).
78. Rosseel, Y. Lavaan: an R package for structural equation modeling. *J. Stat. Softw.* **48**, 1–36 (2012).
79. Petit, J. R. et al. Climate and atmospheric history of the past 420,000 years from the Vostok ice core, Antarctica. *Nature* **399**, 429–436 (1999).
80. Shipley, B. The AIC model selection method applied to path analytic models compared using a d-separation test. *Ecology* **94**, 560–564 (2013).
81. Michael J. Behrenfeld. Abandoning Sverdrup's Critical Depth Hypothesis on phytoplankton blooms. *Ecology* **91**, (4): 977–989 (2010).

### Acknowledgements

We thank all data providers, and N. Yoccoz and K. Ellingson for statistical advice and critical feedback. Funding was provided by the Natural Sciences and Engineering Research Council of Canada (NSERC).

### Author contributions

D.G.B. and B.W. initiated the study. D.G.B. compiled the data, conducted the analyses and wrote the manuscript. B.P., K.T.F. and W.C.L. assisted with the analyses, and all authors discussed the results and edited the manuscript.

### Competing interests

The authors declare no competing financial interests.

### Additional information

**Supplementary information** is available for this paper at doi:10.1038/s41559-017-0287-3.

**Reprints and permissions information** is available at [www.nature.com/reprints](http://www.nature.com/reprints).

**Correspondence and requests for materials** should be addressed to D.G.B.

**Publisher's note:** Springer Nature remains neutral with regard to jurisdictional claims in published maps and institutional affiliations.